Earthquake fingerprint of an incipient subduction of a bathymetric high

Luigi Passarelli[1,2, †,*], Simone Cesca[3], Nima Nooshiri[4], Sigurjón Jónsson[1]

1 King Abdullah University of Science and Technology (KAUST), Thuwal, 23955-6900, Saudi Arabia
2 Swiss Seismological Service, ETH-Zürich, Sonneggstrasse 5, 8092 Zürich, Switzerland
3 GFZ German Research Centre for Geosciences, Telegrafenberg, 14473 Potsdam, Germany
4 DIAS Dublin Institute for Advanced Studies, 10 Burlington Rd, Dublin, D04 C932,
* luigi.passarelli@ingv.it ORCID 0000-0001-8995-8765
† current address: Istituto Nazionale di Geofisica e Vulcanologia, sezione di Bologna, Via Franceschini 31, 40128 Bologna

Key points

An unusually energetic earthquake sequence provides information about the subduction dynamics of the Loyalty Ridge at the Vanuatu trench.

Spatio-temporal patterns of normal faulting earthquakes along the ridge indicate large-scale fracturing in resistance to its subduction.

Ridge subduction leads to low-coupled and locked segments at the interface where M_w8+ earthquakes are unlikely to occur.

Abstract

The resistance of bathymetric highs to subduction results in large-scale morphological distortions of the outer-rise, trench, and fore-arc regions. Once subducted, bathymetric highs induce frictional segmentation along the plate interface that may result in increase or decrease of the plate coupling. However, the mechanics of the collision is inferred mostly from geophysical and geological surveys since earthquakes rarely illuminate finer details of the subduction of seafloor relief. A year-long and energetic seismic sequence at the Loyalty Ridge-Vanuatu Trench allowed us to characterize how strain is released along the collision zone. Earthquakes revealed complex fracturing in the outer-rise and fore-arc regions and segmentation of the interface with both limited magnitude events and aftershock productivity. The complex earthquake activity associated to the collision and subduction of the Loyalty Ridge appears to support a frictionally segmented interface where $M_w \geq 8$ megathrust earthquakes are unlikely to nucleate.

Plain language summary

Subduction zones are regions under the sea where two tectonic plates collide and one plate plunges underneath the other. There, the seafloor of the plunging plate slides and rubs under the overlying plate producing high earthquake activity and large earthquakes called megathrust earthquakes. The seafloor is not everywhere flat, but has kilometer long seamounts in some places that form bathymetric highs. When close to subduction, bathymetric highs resist the

plunging motion and plough through the overlaying plate. This is a catastrophic process that changes both shape of the subduction and associated seismicity. However, it is not well understood whether subducted bathymetric highs can produce large megathrust earthquakes or not. We studied the earthquake activity along the Loyalty Ridge (Pacific Ocean) where it collides and slides underneath the Vanuatu subduction zone. The analysis of the seismicity along the Loyalty Ridge indicates that the earthquakes are caused by the resistance and bending of the ridge due to the subduction motion. At the plates' contact, less earthquakes occur than expected and they are not as large as in the neighboring subduction segments. In this area, with increased damage induced by the plunging ridge, larger megathrust earthquakes (above M_w8) are unlikely to occur.

Introduction

Subduction of bathymetric highs results in structural and frictional variations along the plate boundary that impact how tectonic strain is accumulated and released (Das & Watts, 2009; Wang & Bilek, 2011; Watts et al., 2010). Subducting seamounts and ridges can produce trench indentation, increase the outer rise curvature, and intense fracturing in the overriding plate (Morell, 2016; Taylor et al., 2005; Vannucchi et al., 2013). Once subducted, bathymetric highs modify the interface coupling that can result in increased locking or aseismic creep (Scholz & Small, 1997; Wang & Bilek, 2014). Most of these processes occur over geological time scales and can only be inferred via geomorphological studies and seismic imaging. On rare occasions, however, recorded earthquakes have helped to identify processes related to subduction of bathymetric highs and changes in the frictional properties at the interface (Bell et al., 2014; Morton et al., 2018).

A simple elastic model of a subducting seamount predicts a local normal stress increase due to the elastic response of the overriding plate, resulting in an asperity that can rupture in large-size earthquakes (Cloos, 1992; Scholz & Small, 1997). However, this model defies explanations of the geomorphological and laboratory observations that indicate more complex fracturing of the forearc region as a consequence of subducting bathymetric highs (Dominguez et al., 1998; Ruh et al., 2016; Wang & Bilek, 2011). Laboratory and numerical experiments and observations of scars on the fore-arc seafloor show that the subducting high induces a complex pattern of both compressional and extensional stresses in the overriding plate (Dominguez et al., 1998; von Huene, 2008; Ruh et al., 2016; Sun et al., 2020; Zeumann &

Hampel, 2015). This intense deformation, due to basal erosion (Singh et al., 2011), sediment entrainment (Li et al., 2018), and fracturing of the overriding plate (Ruh et al., 2016), should enhance fluid circulation and could lead to changes of the interface frictional properties, allowing for a wider range of interface behaviors from stable creep to strong locking (Bilek et al., 2003; Collot et al., 2017; Mochizuki et al., 2008).

Global observations highlight the lack of large $M_w \geq 7.5$ megathrust earthquakes at convergent margins with subducting seamounts, ridges and other bathymetric highs (Bassett & Watts, 2015; van Rijsingen et al., 2018). Megathrust regions where bathymetric highs subduct have low interface coupling as a consequence of a fractured overriding plate that hinders large elastic strain to accumulate (Geersen et al., 2015; Marcaillou et al., 2016). The low coupled and segmented interface can host intense foreshock seismicity, repeating earthquakes and aseismic slip (Ruiz et al., 2014; Valenzuela-Malebrán et al., 2021), as well as tremor and very-low frequency events (Todd et al., 2018; Yokota et al., 2016), and it can halt megathrust ruptures (Yokota et al., 2016) or nucleate tsunami earthquakes (Bell et al., 2014). At the Japan trench, an 80-year-long series of repeating interplate $M_w \sim 7$ earthquakes re-ruptured the same interface patch downdip of a creeping seamount (Mochizuki et al., 2008), compatible with an increase of compressive strain at the leading edge of the subducting high (Ruh et al., 2016; Sun et al., 2020). Conversely at the Ecuadorian margin, a seismically imaged subducting relief collocates with a high coupled patch with the potential for hosting $M_w 7+$ megathrusts (Collot et al., 2017). These seismological and geodetic observations highlight a complex pattern of seismic and aseismic strain release at those plate margins characterized by subduction of rough seafloor.

We report on an unusually energetic (10 $M_w 6.5$-7.5) and complex seismic sequence along the collision zone of the Loyalty Ridge (LR) at the Vanuatu Trench (VT) subduction zone that occurred in 2017-2019 (Figs. 1 and 2). The intricate development of large normal faulting seismicity along the outer rise is compatible with fault-assisted subduction of the LR. The earthquakes at the subduction interface suggest a prominent frictional segmentation caused by the LR subduction.

Geological background and past seismicity

The southern VT marks the SW-NE subduction of the Australian plate underneath the North Fiji Basin (Louat & Pelletier, 1989) at a convergence rate of ~120 mm/yr in the ENE direction

along the Vanuatu Archipelago (Fig. 1) (Calmant et al., 2003). The trench-perpendicular convergence slows down to ~40 mm/yr and rotates to a N-S direction at the southern end of the subduction below Matthew and Hunter Islands (Calmant et al., 2003) (Fig. 1a). The LR is a large, 25 km thick and 50 Myr old volcanic arc lying on top of a continental basement (Maurizot et al., 2020) trending N120°E and consists of subparallel horst-and-graben structures bounded by large and steep normal faults (Bogdanov et al., 2011; Lafoy et al., 1996).

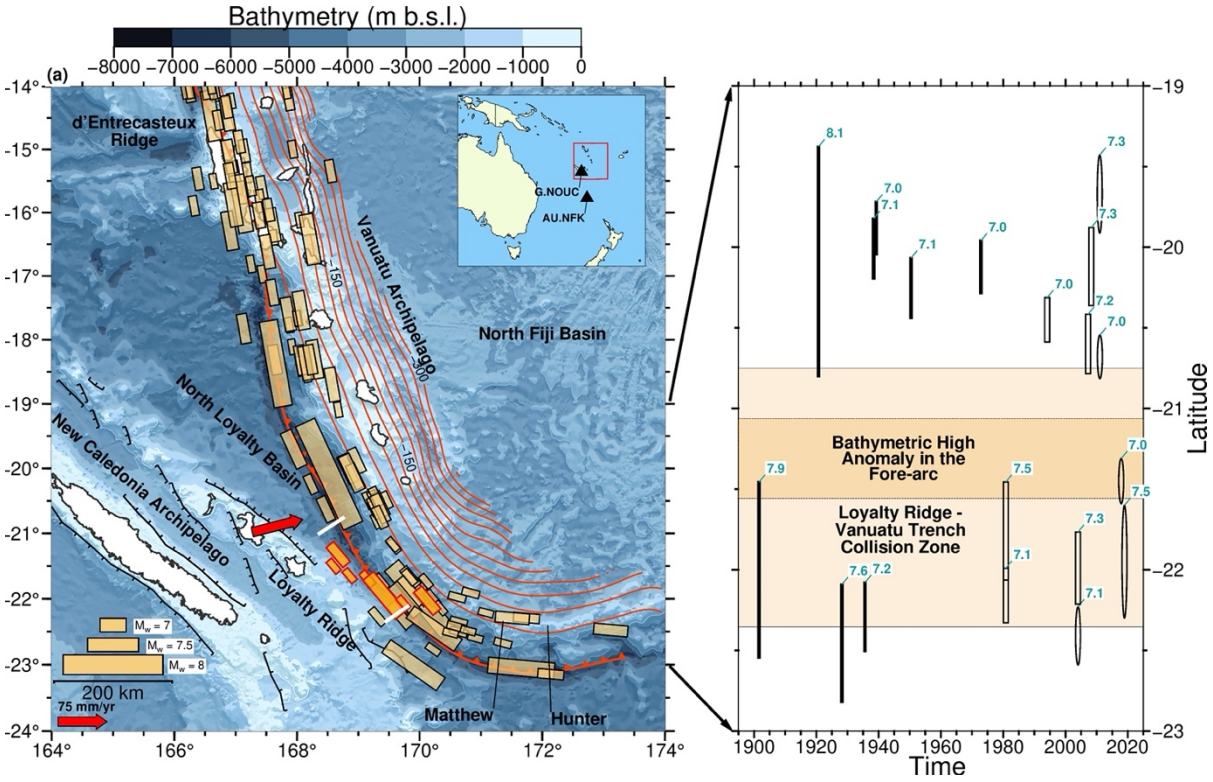

Figure 1. Map of southern Vanuatu subduction and seismicity. a) Rectangles are earthquakes (1900-2021, $M_w \geq 6.5$ and <100 km depth) (ANSS catalog, 2016) whose sides scales with rupture lengths and widths (Thingbaijam et al., 2017). Thicker-outlined rectangles highlight earthquakes of this study (Oct.2017–Feb.2019). Lines are trench and Slab2.0 contours (30km) (Hayes, 2018) and major fault traces (Bogdanov et al., 2011; Lafoy et al., 1996). Red vector indicates velocity of Australian plate for fixed Pacific plate (DeMets et al., 2010) The bathymetry is SRTM30plus (Becker et al., 2009). Two white segments mark the LR-VT-CZ (Monzier et al., 1990). Inset shows the study area (box) and the two seismic stations used in waveform similarity. **b)** Latitude [23S-19S] vs Time for $M_w \geq 7$ earthquakes. Vertical extensions of symbols as in panel a). Vertical bars are earthquakes before 1976, rectangles (thrust) and ellipses (normal) are earthquakes after 1976, and text labels are M_w. Large shaded area indicates latitude of LR-VT-CZ (white segments in panel a)). Small shaded area marks the extension of the residual bathymetric high (Bassett & Watts, 2015) (see also Fig. S1d-f). All symbols are projected onto latitude with an average trench strike 315°.

The increase of the outer rise curvature measured along the Loyalty Archipelago indicates that the north-eastward LR-VT collision (Fig. 1 and S1) started 1-2 Myr B.P. (Dubois et al., 1974) and led to the subduction of the ridge ~0.3-0.5 Myr B.P. (Lafoy et al., 1996). Bathymetric profiles confirm the ridge subduction by a ~1 km topographic resurgence along the trench and

steepening of the LR slope near the trench (Figs. S1 and Fig. 2d). To date, the LR has tunneled obliquely downdip the interface for ~15-45 km (slab dip 10°-20°, plate velocity 50-100 mm/yr for 0.3-0.5 Myr). Analysis of residual bathymetric data along the VT evidences a topographic high in the northern part of the forearc region of the LR-VT collision zone (hereafter LR-VT-CZ) (Fig. 1b and Fig. S1d) (Bassett & Watts 2015). This bathymetric high extends ~50 km trench-perpendicular and ~75 km trench-parallel (Fig. S1e,f) and overlaps with a seismicity gap in the northern segment of the LR-VT-CZ (Figs.1a,b and S1d) that we discuss later. The ~50 km trench-perpendicular extension of the flexural uplift (Fig. S1d) matches well with our kinematic estimation of the LR downdip penetration (~15-45 km). Therefore, the forearc high anomaly is likely the indication of a pronounced penetration of the LR in the north while only incipient in the south of LR-VT-CZ (Fig. S1d,e).

Seismicity recorded since 1900 around the LR-VT-CZ exhibits intense activity that includes two megathrust earthquakes; a M_w7.9 earthquake in 1901 in the south of the LR-VT-CZ, and a M_w8.1 in 1920 located at the southern end of the North Loyalty Basin (Ioualalen et al., 2017; Power et al., 2012) (Figs. 1 and S2). In addition, five $M_w \geq 7$ earthquakes repeatedly broke the south of the LR-VT-CZ (Fig. 1), with a doublet of Mw7.1 and 7.5 occurred 4 hours apart in 1980 (Dziewonski et al., 1981; Ekström et al., 2012) (Fig. 1b). Conversely, the northernmost part of the collision zone has shown only moderate seismicity ($M_w < 7$), exhibiting a notable ~100 km gap of $M_w \geq 7$ earthquakes in a segment that did not break in the two largest megathrust earthquakes in 1901 and 1920 (Fig.1 and S2). Other noticeable events include a M_w7.7 normal faulting earthquake in 1995 along the LR but south of the LR-VT-CZ (Fig. 1a), and a M_w7.1 normal earthquake in 2004 at the southern end of the of LR-VT-CZ (Figs. 1 and S2). Outside the LR-VT-CZ, the largest megathrust ($Mw \geq 7.7$) earthquakes struck in regions characterized by smooth seafloor (van Rijsingen et al., 2018), i.e., south of Matthew and Hunter Islands, in the North Loyalty Basin and north of the d'Entrecasteux Ridge subduction. (Fig. 1a and S2).

The 2017-2019 seismicity in the LR-VT-CZ

We use seismic data from two global earthquake catalogs. A total of 777 were retrieved from the ANSS catalog (USGS Earthquake Hazards Program, 2017) and 192 from the GEOFON Data Center (1993), both having complementary events. The seismicity occurred within a roughly 310 km x 330 km rectangular area (168°-171°E, 20°-23°S) between 31 October 2017

and 28 February 2019. We performed a full moment tensor inversion with a pure double couple constraint (Cesca et al., 2010) and obtained 177 stable focal mechanisms (FMs) with M_w=4.5-7.5 (Fig. 2) that we then classified according to the similarity of the FMs (Cesca, 2020) (see Supplementary material).

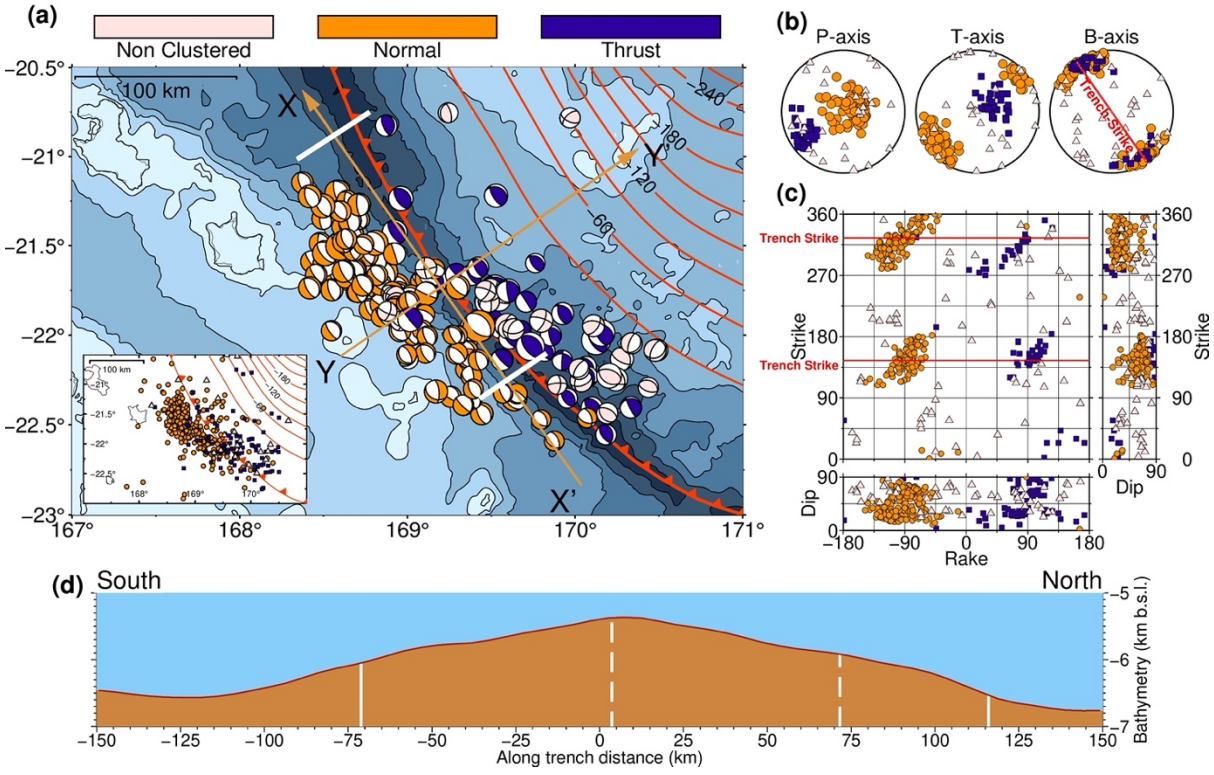

Figure 2. Map of the Oct.2017 – Feb.2019 seismicity along the LR-VT. a) Beach ball focal mechanisms (this study) with size scaling with magnitude and colors for clustered families. Trench line, slab contours, bathymetry, and LR-VT-CZ are as in Fig.1. The cartesian axes X'X (-150,150)km and YY' (-75,150)km are centered at (169.198°E,21.732°S). Inset map shows normal (circles), thrust (squares) and non-clustered (triangles) earthquakes from waveform similarity. **b)** Stereographic plots of the P-, T- and B-axes of the 177 FMs shown in a), the red-line is the trench strike direction. **c)** Strike, rake and dip for both focal planes of the 177 FMs in main panel a), and red-lines are trench strike directions. **d)** Bathymetry profile (in km b.s.l. in the X'X-YY' Cartesian system in panel a)) of a 5km swath centered along the curved trench line and low-pass filtered at 100 km (Savitzky-Golay moving average). Vertical solid and dashed lines delineate LR-VT-CZ and fore-arc bathymetric high anomaly (Bassett & Watts, 2015), respectively (see Fig.1b and S1d-f).

Three main families of events were identified: a cluster of 114 normal faulting earthquakes, one with 34 thrust mechanisms, while the remaining non-clustered 29 have both large strike and rake variability (Figs. 2a-c and S3). To extend the source analysis to smaller events, we pair-wise cross-correlated the waveform of each of the 177 FMs to the remaining earthquakes in both the ANSS and GEOFON catalogs (Fig. S4) using recordings at two nearby stations (Fig. 1a). This procedure allowed to further categorize 441 events (cross-correlation>0.9, Fig. S4) to one of the three previously identified families of events (Fig. 2a). We also attempted to

relocate the earthquakes using a relocation algorithm (Nooshiri et al., 2017) and the LLNL-G3Dv3 3D velocity model (Simmons et al., 2012), but without achieving a satisfactory improvement on the earthquake hypocenters (see Supplement Material and Figs. S6). Therefore, for consistency, we opted to use the ANSS catalog epicenters that have horizontal errors of 2-25 km with a median of 7 km. The earthquake depths (5-45 km) in the catalog are, however, poorly constrained and so are the depths of our relocated events (depths 0-50 km) (Fig. S5). The determined FM centroid depths, also poorly resolved, indicate that the earthquakes were systematically shallow at depths of 0-25 km (Fig. S7).

The P-, T- and B-axis distribution indicate seismicity controlled by compression at the subduction interface (thrust faulting) and by extension in the outer rise (normal faulting) (Fig. 2b). In Fig. 2c, the thrust FMs are within ±20° of the average trench strike (N145°±10°E) and the strikes of the normal-faulting FMs, while more variable, match the orientation of mapped faults sub-parallel to the ridge axis in the LR-VT-CZ (Fig. 1) (Bogdanov et al., 2011; Monzier et al., 1990). Focal planes of reverse FMs that are eastward and shallowly dipping (~10°-30°) are compatible with activity at the slab interface (Fig. 2c). Steep planes (dip ~50°- 85°) of the normal-faulting FMs, both westward and eastward dipping, are in accordance with the steeply dipping faults mapped across the LR, similar to other outer rise regions (Craig et al., 2014) (Fig. 2c). The smaller and non-categorized events indicate a range of other fault orientations at the plate boundary, a complexity that indicates complex fracturing in the overriding plate (Fig. 2a and 3).

From October 2017 and until February 2019 the seismicity in the LR-VT region evolved in four distinct temporal phases (Figs. 3 and 4a-d). Phase 1 started with a M_w6.8 tsunamigenic thrust earthquake on the 31 October 2017 (Figs. 3 and 4a) whose location and shallow focal plane (dip=25°) are compatible with a rupture at the interface (slab dip=10°-20°) (Fig. 2), although we cannot completely exclude that the earthquake occurred on the steep thrust faults in the compressional accretionary trench outer-wall (Monzier et al., 1990). This thrust event was followed by a month-long swarm of normal-faulting earthquakes (10 events with M_w>6) illuminating ~100x80 km^2 area of the LR (Fig. 3). Within the first 24 hours, three large normal events (M_w>6) occurred with the largest M_w6.7 triggering another small tsunami (Roger et al., 2019) (Figs. 3 and 4a). The seismicity then gradually expanded northward, where on 19 November a M_w7 earthquake struck a few hours after two M_w6.3 and 6.7 events (Figs. 3 and

4a). Almost no thrust earthquakes occurred on the subduction interface after the first M_w6.8 thrust event at the beginning of Phase 1 (Figs. 3 and 4a).

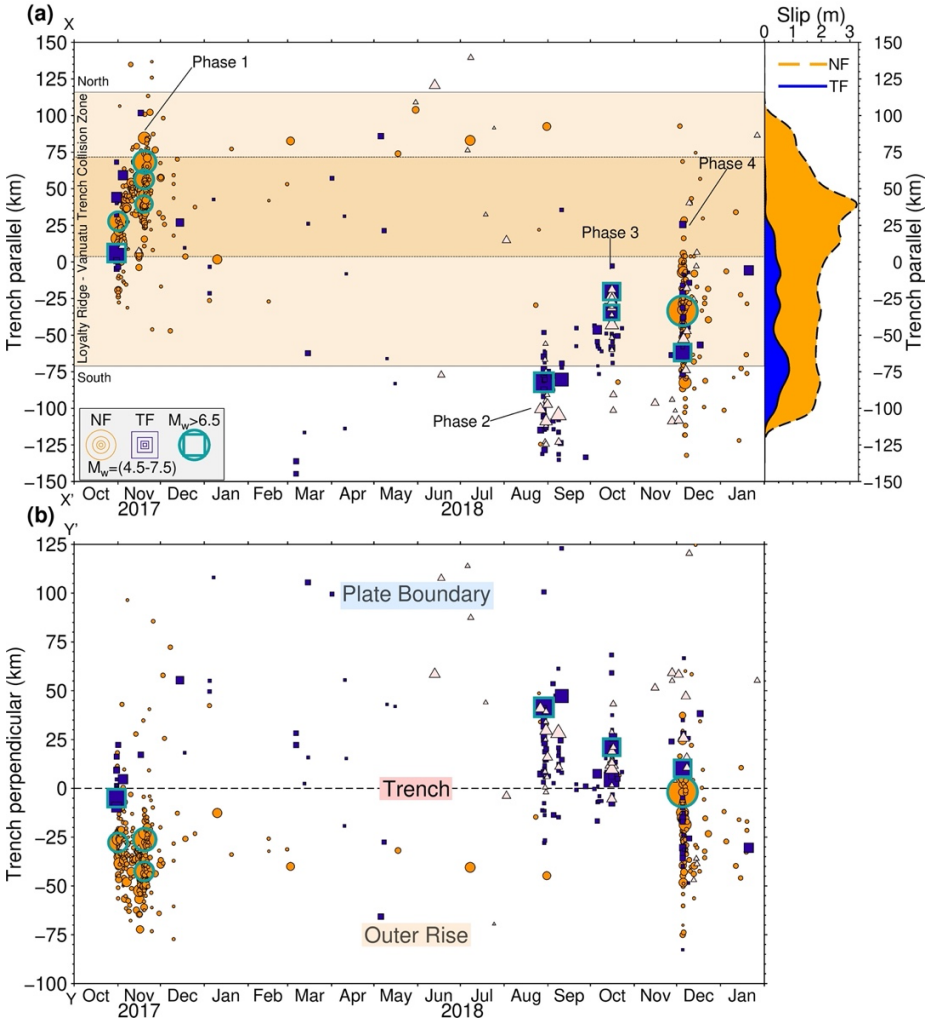

Figure 3. Earthquake epicenters vs time of occurrence along and across the LR-VT region. **(a)** Trench-parallel event locations vs time with circles (normal fault), squares (thrust fault) and triangles (non-clustered) color-coded as in Fig. 2. Symbol sizes scale with magnitude (see legend). Thicker outlined symbols are events of M_w>6.5 discussed in the text. Large and small shaded areas as in Fig. 1b. Cumulative seismic slip is in the right-hand panel (see Supplementary Material). **(b)** Same as panel a) for trench perpendicular locations vs time with the outer rise (y<0) and plate boundary (y>0), and trench (y=0) regions indicated. Here earthquake *y*-coordinates are corrected for the trench curvature with respect to axis YY' in Fig. 2a.

After a relatively quiet 9-month period, Phase 2 (Fig. 4b) started on 29 August 2018 with a large tsunamigenic M_w6.9 thrust event that occurred 100 km south of the earthquake at the start of Phase 1 and was followed by aftershocks until mid-September (Figs. 3 and 4b). About a month later, in phase 3 (Fig. 4c) the activity jumped ~50 km north where on 16 October, a M_w6.5 and 6.7 thrust doublet occurred one hour apart (Figs. 3 and 4c) followed by a short-lasting aftershock activity (Fig. 3). Phase 4 (Fig. 4d) started on 5 December with a large M_w7.5 normal-faulting earthquake, anticipated by 3.5 minutes by an identical M_w6 foreshock

(undetected by global agency), and followed two hours later by a M_w6.9 thrust aftershock at the subduction interface (Figs. 3 and 4d). The M_w7.5 generated a large tsunami and caused aftershocks in the entire LR-VT outer rise segment as well as along the slab interface (Fig. 3a). The cumulative average slip (Fig. 3a) indicates normal faulting occurred along a ~200 km long section of the LR but a lack of reverse slip in the northern segment of the LR-VT-CZ (see Fig. 2a and Supplementary Material).

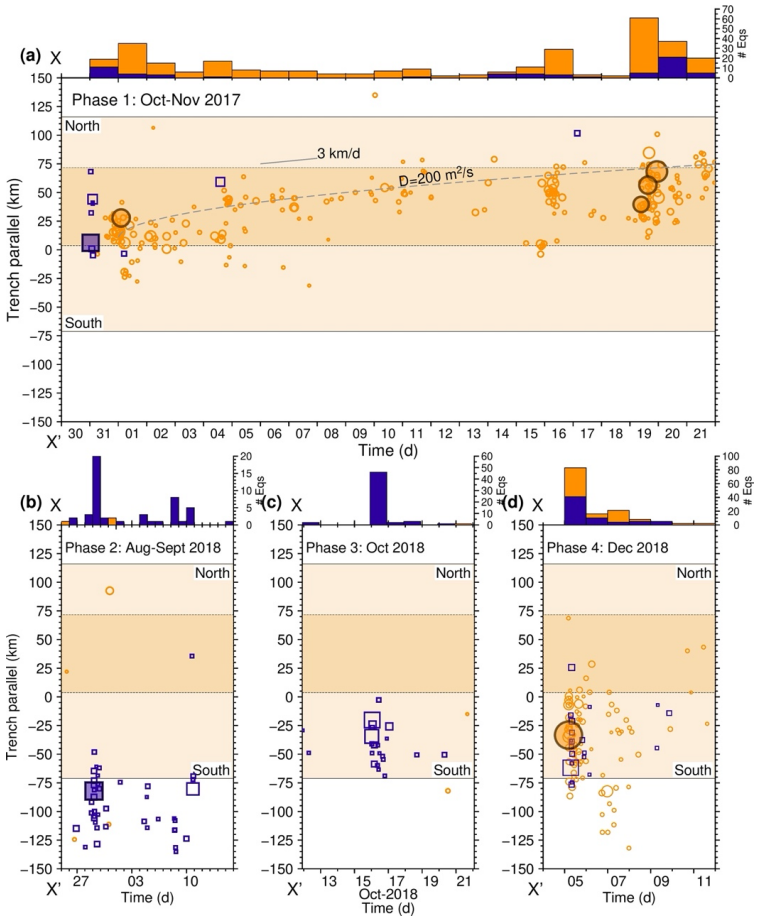

Figure 4. Earthquake locations along trench vs time of occurrence for normal- and thrust-faulting events. Panels (a)-(d) are the four activity phases discussed in the text and highlighted in Fig. 3a. Symbols and color-code are as in Fig. 3. Thicker-outlined symbols are tsunamigenic earthquakes. Number of earthquakes per day are indicated in the above histograms. In panel (a), the thin dashed line is pore-pressure diffusion fit and the solid line indicates migration velocity. Large and small shaded areas as in Fig. 1b.

Seismicity unveils mechanisms of the ridge subduction

The uniform normal-fault slip release along the LR (phases 1 and 4) suggest frictional variability of the ruptured faults that developed through a migrating swarm-like sequence in the north and a single M_w7.5 in the south (Fig. 4a). In both segments, the two largest Mw7+ likely ruptured the whole 25 km of crustal thickness of LR (Maurizot et al., 2020). In addition, the overlap of ruptures along the trench (Fig. 4) and their extent across the ~80 km wide LR

(Fig. 3b) indicate the activation of the whole outer rise fault system. The complex source time functions of largest normal earthquakes (Vallée et al., 2011) (Fig. S8a) and the swarm-like characteristic of seismicity supports frictional variability of the LR normal fault system. The compositional heterogeneities of the ridge crust (Maurizot et al., 2020) and the asymmetric bending deformation induced by the oblique collision can probably explain the differences in the fault slip release via earthquake swarm in the north and a single M_w7.5 in the south (Fig. 3 and 4). Moreover, the locations of two M_w>7 earthquakes close to the trench (Fig. 3b) suggest that the largest amount of slip focused on ridge-bounding faults (Lafoy et al., 1996). This can likely be to accommodate the incipient subduction of the LR via normal faulting as similarly was suggested from geomorphological investigation of the incipient subduction of the Daiichi-Kashima seamount in Japan (Lallemand et al., 1989).

Reverse slip at the subduction interface unclamps the normal faults in the outer rise promoting seismicity (Sladen & Trevisan, 2018). Similarly, normal ruptures in the outer rise transfer positive Coulomb Failure Stress changes (ΔCFS) on the plate interface (Ogata & Toda, 2010). We verified the mutual positive ΔCFS transfer of a thrust event on the interface onto a normal fault in the outer rise and vice versa (Fig. S9). The static stress transfer can thus explain the mutual triggering between thrust and normal faulting activity and the trench parallel evolution of the seismicity. In particular, for phase 1, the km/day expansion of seismicity cannot be explained with a pore-pressure diffusion model, because the inferred permeability (diffusivity ~200 m^2/s, see Fig. 4a) would be unrealistically high (Talwani et al., 2007). The expansion of the seismicity front along the LR (Fig. 3a and b) seems instead to indicate a gradual and fast flexural fracturing of the LR, driven by incremental increase of ΔCFS beyond the edges of the earthquake ruptures. The large accrued flexural stresses (Bogdanov et al., 2011), low friction coefficient (Craig et al., 2014), and abundance of crustal fluids (Ranero et al., 2003) of the outer rise faults might have facilitated this propagation mechanism.

At the plate boundary, the seismicity shows lower activity and uneven slip distribution (Fig. 3d). The fit of Omori-Utsu law for large thrust and normal events either fails to and/or overpredicts the observed low aftershock rate (Fig. S10). The extremely low number of aftershocks of the first M_w6.8 thrust is remarkable (Fig. 4 and S10a) and locates in the seismicity gap along the interface (Fig. 1), although the synchronous normal earthquake swarm activity continuously transferred positive ΔCFS back onto the interface (Fig. S9). Low aftershock productivity is consistent with nucleation of tsunamigenic earthquakes in frictional

conditionally stable regions along the interface (Scholz, 1998). Here, velocity weakening asperities loaded by the rupture release completely the accrued stresses and limit the aftershock productivity (Polet & Kanamori, 2000). The LR subduction in the north of LR-VT-CZ (Figs. 1 and S1d) produces rough and weakly coupled interface, the ideal habitat to reduce the amount of fracture energy released seismically. The multiple peaks and long duration of the moment-rate distribution of thrust events (Fig S8) support the above scenario.

Reduced elastic strain accumulation at the interface is expected where a seamount subducts due to the intense deformation of the fore-arc (Wang & Bilek 2011). The resulting low-coupled megathrust can host slow slip transients and stop large megathrust ruptures (Geersen et al., 2015; Ruiz et al., 2014). The forearc uplift at the northernmost part of LR-VT-CZ (Bassett & Watts, 2015) (Figs.1b and S1d) coincides with the interface segment with a lack of M_w7+ thrust earthquakes, low aftershocks productivity and the stop of the 1901, 1920 and 1980 M_w~8 ruptures (Fig. 1 and S2). Here, plate convergence is likely accommodated via creep or episodic slow slip, and only a relatively small amount of slip is released seismically (Fig. 3a). Conversely, the southern segment of the interface — where the LR penetration is incipient — is repeatedly ruptured by frequent Mw7+ earthquakes (Fig. 1b). Such intense thrust activity is compatible with compressive stresses imparted onto the interface by the leading edge of the LR, as observed in Japan (Mochizuki et al., 2008) and predicted by numerical models (Ruh et al., 2016; Sun et al., 2020). Moreover, the oblique ridge subduction (Shulgin et al., 2011; Zeumann & Hampel, 2015) generates a complex stress field in the fore-arc that matches well with the heterogeneous and small magnitude focal mechanisms located there (non-clustered events in Fig. 2a). However, we cannot completely exclude that the heterogeneous mechanisms represent activation of conjugate splay faults in the overriding plate.

Conclusions

We have demonstrated that the collision and subduction of the LR along VT result in a complex release of tectonic strain. The swarm-like activity on the northern segment of the LR can be indicative of the flexural fracturing driven by static stress transfer and low effective friction along a lubricated outer rise fault system. In the northern sector of the LR, large slip on normal faults also occurs close to the trench to largely accommodate the subduction of the ridge and uniform normal slip release implies a homogeneous accumulation of stresses along the LR. At the plate boundary, a frictionally segmented interface induced by the ridge subduction is

supported by a persistent M_w7+ gap and repeated equally-sized M_w7 earthquakes in the north and south of LR-VT-CZ, respectively. This ridge-trench collision and interaction are far more complex than a simple increase of elastic coupling along the interface and favor the hypothesis of a complex and segmented interface where M_w8+ megathrust earthquakes are unlikely to nucleate.

Acknowledgements

This research was supported by King Abdullah University of Science and Technology (KAUST) under the award OSR-2016-CRG6-3027-01. LP acknowledge funds from the project DEEP-GEOTHERMICA.

Open Research

Seismic data used in this study are open and available at IRIS (https://service.iris.edu/fdsnws/), GEOFON (https://geofon.gfz-potsdam.de/waveform/webservices/fdsnws.php) and ORFEUS (https://www.orfeus-eu.org/data/eida/webservices/) data centers through FDSN web service. Seismicity catalogs and phase arrival time can be downloaded at https://earthquake.usgs.gov/earthquakes/search/ (ANSS-USGS) and https://geofon.gfz-potsdam.de/eqinfo/list.php (GEOFON). Software used for analysis of seismic data is open source and available at: Seiscloud (Cesca, 2020) (https://git.pyrocko.org/cesca/seiscloud/), Scoter (Nooshiri et al., 2019) and Pyrocko (Heimann et al., 2017) (https://pyrocko.org/).

Bassett, D., & Watts, A. B. (2015). Gravity anomalies, crustal structure, and seismicity at subduction zones: 1. Seafloor roughness and subducting relief. *Geochemistry, Geophysics, Geosystems*, *16*(5). https://doi.org/10.1002/2014GC005684

Becker, J. J., Sandwell, D. T., Smith, W. H. F., Braud, J., Binder, B., Depner, J., et al. (2009). Global Bathymetry and Elevation Data at 30 Arc Seconds Resolution: SRTM30_PLUS. *Marine Geodesy*, *32*(4). https://doi.org/10.1080/01490410903297766

Bell, R., Holden, C., Power, W., Wang, X., & Downes, G. (2014). Hikurangi margin tsunami earthquake generated by slow seismic rupture over a subducted seamount. *Earth and Planetary Science Letters*, *397*. https://doi.org/10.1016/j.epsl.2014.04.005

Bilek, S. L., Schwartz, S. Y., & DeShon, H. R. (2003). Control of seafloor roughness on earthquake rupture behavior. *Geology*, *31*(5), 455. https://doi.org/10.1130/0091-7613(2003)031<0455:COSROE>2.0.CO;2

Bogdanov, I., Huaman, D., Thovert, J. F., Genthon, P., & Adler, P. M. (2011). Tectonic stresses seaward of an aseismic ridge-Trench collision zone. A remote sensing approach on the Loyalty Islands, SW Pacific. *Tectonophysics*, *499*(1–4), 77–91. https://doi.org/10.1016/j.tecto.2010.12.007

Calmant, S., Pelletier, B., Lebellegard, P., Bevis, M., Taylor, F. W., & Phillips, D. A. (2003). New insights on the tectonics along the New Hebrides subduction zone based on GPS results. *Journal of Geophysical Research: Solid Earth*, *108*(B6), 1–22. https://doi.org/10.1029/2001jb000644

Cesca, S. (2020). Seiscloud, a tool for density-based seismicity clustering and visualization. *Journal of Seismology*, *24*(3). https://doi.org/10.1007/s10950-020-09921-8

Cesca, S., Heimann, S., Stammler, K., & Dahm, T. (2010). Automated procedure for point and kinematic source inversion at regional distances. *Journal of Geophysical Research: Solid Earth*, *115*(6), B06304. https://doi.org/10.1029/2009JB006450

Cloos, M. (1992). Thrust-type subduction-zone earthquakes and seamount asperities: a physical model for seismic rupture. *Geology*, *20*(7), 601–604. https://doi.org/10.1130/0091-7613(1992)020<0601:TTSZEA>2.3.CO;2

Collot, J. Y., Sanclemente, E., Nocquet, J. M., Leprêtre, A., Ribodetti, A., Jarrin, P., et al. (2017). Subducted oceanic relief locks the shallow megathrust in central Ecuador. *Journal of Geophysical Research: Solid Earth*, *122*(5). https://doi.org/10.1002/2016JB013849

Craig, T. J., Copley, A., & Middleton, T. A. (2014). Constraining fault friction in oceanic lithosphere using the dip angles of newly-formed faults at outer rises. *Earth and Planetary Science Letters*, *392*, 94–99. https://doi.org/10.1016/j.epsl.2014.02.024

Das, S., & Watts, A. B. (2009). Effect of Subducting Seafloor Topography on the Rupture Characteristics of Great Subduction Zone Earthquakes (pp. 103–118). https://doi.org/10.1007/978-3-540-87974-9_6

DeMets, C., Gordon, R. G., & Argus, D. F. (2010). Geologically current plate motions. *Geophysical Journal International*. https://doi.org/10.1111/j.1365-246X.2009.04491.x

Dominguez, S., Lallemand, S. E., Malavieille, J., & von Huene, R. (1998). Upper plate deformation associated with seamount subduction. *Tectonophysics*, *293*(3–4), 207–224. https://doi.org/10.1016/S0040-1951(98)00086-9

Dubois, J., Launay, J., & Recy, J. (1974). Uplift movements in New Caledonia-Loyalty Islands area and their plate tectonics interpretation. *Tectonophysics*, *24*(1–2). https://doi.org/10.1016/0040-1951(74)90134-6

Dziewonski, A. M., Chou, T. A., & Woodhouse, J. H. (1981). Determination of earthquake source parameters from waveform data for studies of global and regional seismicity. *Journal of Geophysical Research*, *86*(B4). https://doi.org/10.1029/JB086iB04p02825

Ekström, G., Nettles, M., & Dziewoński, A. M. (2012). The global CMT project 2004-2010: Centroid-moment tensors for 13,017 earthquakes. *Physics of the Earth and Planetary Interiors*, *200–201*, 1–9. https://doi.org/10.1016/j.pepi.2012.04.002

Geersen, J., Ranero, C. R., Barckhausen, U., & Reichert, C. (2015). Subducting seamounts control interplate coupling and seismic rupture in the 2014 Iquique earthquake area. *Nature Communications*, *6*. https://doi.org/10.1038/ncomms9267

GEOFON Data Center. (1993). GEOFON Seismic Network,Deutsches GeoForschungsZentrum GFZ. Other/Seismic Network. https://doi.org/10.14470/TR560404

Hayes, G. (2018). *Slab2 - A Comprehensive Subduction Zone Geometry Model:* https://doi.org/https://doi.org/10.5066/F7PV6JNV

Heimann, S., Kriegerowski, M., Isken, M., Cesca, S., Daout, S., Grigoli, F., et al. (2017). Pyrocko - An open-source seismology toolbox and library. GFZ Data Services. https://doi.org/10.5880/GFZ.2.1.2017.001

von Huene, R. (2008). When Seamounts Subduct. *Science*, *321*(5893), 1165–1166. Retrieved from http://www.sciencemag.org/content/321/5893/1165.short

Ioualalen, M., Pelletier, B., & Solis Gordillo, G. (2017). Investigating the March 28th 1875 and the September 20th 1920 earthquakes/tsunamis of the Southern Vanuatu arc, offshore Loyalty Islands, New Caledonia. *Tectonophysics*, *709*, 20–38. https://doi.org/10.1016/j.tecto.2017.05.006

Lafoy, Y., Missegue, F., Cluzel, D., & le Suave, R. (1996). The Loyalty-New Hebrides arc collision: Effects on the loyalty ridge and basin system, Southwest Pacific (first results of the ZoNéCo programme). *Marine Geophysical Research*, *18*(2–4), 337–356. https://doi.org/10.1007/BF00286084

Lallemand, S., Culotta, R., & von Huene, R. (1989). Subduction of the Daiichi Kashima Seamount in the Japan Trench. *Tectonophysics*, *160*(1–4), 231–241. https://doi.org/10.1016/0040-1951(89)90393-4

Li, J., Shillington, D. J., Saffer, D. M., Bécel, A., Nedimović, M. R., Kuehn, H., et al. (2018). Connections between subducted sediment, pore-fluid pressure, and earthquake behavior along the Alaska megathrust. *Geology*, *46*(4). https://doi.org/10.1130/G39557.1

Louat, R., & Pelletier, B. (1989). Seismotectonics and present-day relative plate motions in the New Hebrides - North Fiji Basin region. *Tectonophysics*, *167*(1), 41–55. https://doi.org/10.1016/0040-1951(89)90293-X

Marcaillou, B., Collot, J.-Y., Ribodetti, A., d'Acremont, E., Mahamat, A.-A., & Alvarado, A. (2016). Seamount subduction at the North-Ecuadorian convergent margin: Effects on structures, inter-seismic coupling and seismogenesis. *Earth and Planetary Science Letters*, *433*, 146–158. https://doi.org/10.1016/j.epsl.2015.10.043

Maurizot, P., Collot, J., Cluzel, D., & Patriat, M. (2020). The loyalty islands and ridge, New Caledonia. In *Geological Society Memoir* (Vol. 51). https://doi.org/10.1144/M51-2017-24

Mochizuki, K., Yamada, T., Shinohara, M., Yamanaka, Y., & Kanazawa, T. (2008). Weak interplate coupling by seamounts and repeating M ~ 7 earthquakes. *Science*, *321*(5893), 1194–1197. https://doi.org/10.1126/science.1160250

Monzier, M., Daniel, J., & Maillet, P. (1990). La collision "ride des Loyauté/ arc des Nouvelles-Hébrides" (Pacifique Sud-Ouest). *Oceanologica Acta*, *10*(43–56). Retrieved from http://www.documentation.ird.fr/hor/fdi:31937

Morell, K. D. (2016). Seamount, ridge, and transform subduction in southern Central America. *Tectonics*, *35*(2). https://doi.org/10.1002/2015TC003950

Morton, E. A., Bilek, S. L., & Rowe, C. A. (2018). Newly detected earthquakes in the Cascadia subduction zone linked to seamount subduction and deformed upper plate. *Geology*, *46*(11). https://doi.org/10.1130/G45354.1

Nooshiri, N., Saul, J., Heimann, S., Tilmann, F., & Dahm, T. (2017). Revision of earthquake hypocentre locations in global bulletin data sets using source-specific station terms. *Geophysical Journal International*, *208*(2). https://doi.org/10.1093/gji/ggw405

Nooshiri, N., Heimann, S., Tilmann, F., Dahm, T., & Saul, J. (2019). SCOTER - Software package for multiple-earthquake relocation by using static and source-specific station correction terms. V. 0.1. GFZ Data Services. https://doi.org/10.5880/GFZ.2.1.2019.002

Ogata, Y., & Toda, S. (2010). Bridging great earthquake doublets through silent slip: On- and off-fault aftershocks of the 2006 Kuril Island subduction earthquake toggled by a slow slip on the outer rise normal fault of the 2007 great earthquake. *Journal of Geophysical Research: Solid Earth*, *115*(6), 1–15. https://doi.org/10.1029/2009JB006777

Polet, J., & Kanamori, H. (2000). Shallow subduction zone earthquakes and their tsunamigenic potential. *Geophysical Journal International*. https://doi.org/10.1046/j.1365-246X.2000.00205.x

Power, W., Wallace, L., Wang, X., & Reyners, M. (2012). Tsunami hazard posed to New Zealand by the Kermadec and southern New Hebrides subduction margins: An assessment based on plate boundary kinematics, interseismic coupling, and historical seismicity. *Pure and Applied Geophysics*, *169*(1–2), 1–36. https://doi.org/10.1007/s00024-011-0299-x

Ranero, C. R., Morgan, J. P., McIntosh, K. D., & Reichert, C. (2003). Flexural faulting and mantle serpentinization at the Middle American. *Nature*, *425*, 367–373.

van Rijsingen, E., Lallemand, S., Peyret, M., Arcay, D., Heuret, A., Funiciello, F., & Corbi, F. (2018). How Subduction Interface Roughness Influences the Occurrence of Large Interplate Earthquakes. *Geochemistry, Geophysics, Geosystems*, *19*(8). https://doi.org/10.1029/2018GC007618

Roger, J., Pelletier, B., & Aucan, J. (2019). Update of the tsunami catalogue of New Caledonia using a decision table based on seismic data and maregraphic records. *Natural Hazards and Earth System Sciences Discussions*, 1–22. https://doi.org/10.5194/nhess-2019-36

Ruh, J. B., Sallarès, V., Ranero, C. R., & Gerya, T. (2016). Crustal deformation dynamics and stress evolution during seamount subduction: High-resolution 3-D numerical modeling. *Journal of Geophysical Research: Solid Earth*, *121*(9). https://doi.org/10.1002/2016JB013250

Ruiz, S., Metois, M., Fuenzalida, A., Ruiz, J., Leyton, F., Grandin, R., et al. (2014). Intense foreshocks and a slow slip event preceded the 2014 Iquique Mw 8.1 earthquake. *Science*, *345*(6201), 1165–1169. https://doi.org/10.1126/science.1256074

Scholz, C. H. (1998). Earthquakes and friction laws. *Nature*. https://doi.org/10.1038/34097

Scholz, C. H., & Small, C. (1997). The effect of seamount subduction on seismic coupling. *Geology*, *25*(6), 487–490. https://doi.org/10.1130/0091-7613(1997)025<0487:TEOSSO>2.3.CO;2

Shulgin, A., Kopp, H., Mueller, C., Planert, L., Lueschen, E., Flueh, E. R., & Djajadihardja, Y. (2011). Structural architecture of oceanic plateau subduction offshore Eastern Java and the potential implications for geohazards. *Geophysical Journal International*, *184*(1). https://doi.org/10.1111/j.1365-246X.2010.04834.x

Simmons, N. A., Myers, S. C., Johannesson, G., & Matzel, E. (2012). LLNL-G3Dv3: Global P wave tomography model for improved regional and teleseismic travel time prediction. *Journal of Geophysical Research: Solid Earth*, *117*(10). https://doi.org/10.1029/2012JB009525

Singh, S. C., Hananto, N., Mukti, M., Robinson, D. P., Das, S., Chauhan, A., et al. (2011). Aseismic zone and earthquake segmentation associated with a deep subducted seamount in Sumatra. *Nature Geoscience*, *4*(5), 308–311. https://doi.org/10.1038/ngeo1119

Sladen, A., & Trevisan, J. (2018). Shallow megathrust earthquake ruptures betrayed by their outer-trench aftershocks signature. *Earth and Planetary Science Letters*, *483*, 105–113. https://doi.org/10.1016/j.epsl.2017.12.006

Sun, T., Saffer, D., & Ellis, S. (2020). Mechanical and hydrological effects of seamount subduction on megathrust stress and slip. *Nature Geoscience*, *13*(3). https://doi.org/10.1038/s41561-020-0542-0

Talwani, P., Chen, L., & Gahalaut, K. (2007). Seismogenic permeability, ks. *Journal of Geophysical Research: Solid Earth*, *112*(7), B07309. https://doi.org/10.1029/2006JB004665

Taylor, F. W., Mann, P., Bevis, M. G., Edwards, R. L., Cheng, H., Cutler, K. B., et al. (2005). Rapid forearc uplift and subsidence caused by impinging bathymetric features: Examples from the New Hebrides and Solomon arcs. *Tectonics*, *24*(6), 1–23. https://doi.org/10.1029/2004TC001650

Thingbaijam, K. K. S., Mai, P. M., & Goda, K. (2017). New empirical earthquake source-scaling laws. *Bulletin of the Seismological Society of America*, *107*(5), 2225–2246. https://doi.org/10.1785/0120170017

Todd, E. K., Schwartz, S. Y., Mochizuki, K., Wallace, L. M., Sheehan, A. F., Webb, S. C., et al. (2018). Earthquakes and Tremor Linked to Seamount Subduction During Shallow Slow Slip at the Hikurangi Margin, New Zealand. *Journal of Geophysical Research: Solid Earth*, *123*(8), 6769–6783. https://doi.org/10.1029/2018JB016136

USGS Earthquake Hazards Program. (2017). Advanced National Seismic System (ANSS) Comprehensive Catalog of Earthquake Events and Products: Various,. https://doi.org/https://doi.org/10.5066/F7MS3QZH

Valenzuela-Malebrán, C., Cesca, S., Ruiz, S., Passarelli, L., Leyton, F., Hainzl, S., et al. (2021). Seismicity clusters in Central Chile: Investigating the role of repeating earthquakes and swarms in a subduction region. *Geophysical Journal International*, *224*(3). https://doi.org/10.1093/gji/ggaa562

Vallée, M., Charléty, J., Ferreira, A. M. G., Delouis, B., & Vergoz, J. (2011). SCARDEC: A new technique for the rapid determination of seismic moment magnitude, focal mechanism and source time functions for large earthquakes using body-wave deconvolution. *Geophysical Journal International*, *184*(1). https://doi.org/10.1111/j.1365-246X.2010.04836.x

Vannucchi, P., Sak, P. B., Morgan, J. P., Ohkushi, K., & Ujiie, K. (2013). Rapid pulses of uplift, subsidence, and subduction erosion offshore central america: Implications for building the rock record of convergent margins. *Geology*, *41*(9). https://doi.org/10.1130/G34355.1

Wang, K., & Bilek, S. L. (2011). Do subducting seamounts generate or stop large earthquakes? *Geology*, *39*(9), 819–822. https://doi.org/10.1130/G31856.1

Wang, K., & Bilek, S. L. (2014). Invited review paper: Fault creep caused by subduction of rough seafloor relief. *Tectonophysics*, *610*, 1–24. https://doi.org/10.1016/j.tecto.2013.11.024

Watts, A. B., Koppers, A. A. P., & Robinson, D. P. (2010). Seamount subduction and earthquakes. *Oceanography*, *23*(1), 166–173. https://doi.org/10.5670/oceanog.2010.68

Yokota, Y., Ishikawa, T., Watanabe, S. I., Tashiro, T., & Asada, A. (2016). Seafloor geodetic constraints on interplate coupling of the Nankai Trough megathrust zone. *Nature*, *534*(7607), 374–377. https://doi.org/10.1038/nature17632

Zeumann, S., & Hampel, A. (2015). Deformation of erosive and accretive forearcs during subduction of migrating and non-migrating aseismic ridges: Results from 3-D finite element models and application to the Central American, Peruvian, and Ryukyu margins. *Tectonics*, *34*(9). https://doi.org/10.1002/2015TC003867